Check for updates

Interaction of anionic Fe$_3$O$_4$ nanoparticles with lipid vesicles: a review on deformation and poration under various conditions

Mohammad Abu Sayem Karal, [ID] *[a] Md. Masum Billah, [ID] *[b] Tawfika Nasrin[a] and Md. Moniruzzaman [ID] [a]

This review focuses on the deformation and poration of lipid vesicles caused by the interaction of anionic magnetite nanoparticles (MNPs). Effects of various factors, such as surface charge density, salt and sugar concentrations in buffer, membrane cholesterol content, polymer–grafted phospholipid, and membrane potential have been discussed for the interaction of MNPs with lipid vesicles. To quantify these effects on the vesicles, compactness, fraction of deformation and poration, dynamics of membrane permeation, and kinetics of membrane permeation have been critically evaluated. The review explores the potential advancements as well as future directions of the research field in the biomedical application of MNPs.

1. Introduction

Nanoparticles are considered to be potential biomedical tools, offering promise in both diagnostic and therapeutic endeavors due to their adaptability and compatibility with biological systems.[1–5] Magnetite nanoparticles (Fe$_3$O$_4$; MNPs) exhibit promising applications in various fields including MRI contrast, precious delivery of drugs, bacteria identification, cell labeling, bioseparation, and anticancer therapy due to their physical and chemical properties.[6–11] For instance, MNPs can be enveloped with either pharmaceutical compounds or biomolecules to facilitate interaction with, or binding to, specific biological targets, thus enhancing their suitability for various medical interventions.[12–15] However, the adverse effects of the NPs have also been reported.[16–21] MNPs are found in the environment from natural sources like volcanic eruptions and meteorite impacts, and from human activities such as industrial processes, power plants, and marine seeds.[22,23] The presence of MNPs potentially impacts human health and the environment.[21] Depending on the MNPs size, shape and

[a]*Department of Physics, Bangladesh University of Engineering and Technology, Dhaka 1000, Bangladesh. E-mail: asayem221@phy.buet.ac.bd; Fax: +880-2-58613046; Tel: +880-2-9665613*

[b]*Department of Physics, Jashore University of Science and Technology, Jashore 7408, Bangladesh. E-mail: mm.billah@just.edu.bd; Fax: +880-2-42142012; Tel: +880-242142046*

Mohammad Abu Sayem Karal is a Professor in the Department of Physics at Bangladesh University of Engineering and Technology, Bangladesh. He obtained his PhD from Shizuoka University, Japan, specializing in membrane biophysics. His research focuses on elucidating the mechanisms of lipid membrane rupture and pore formation induced by nanoparticles, irreversible electroporation, micropipette aspiration, and antimicrobial peptides.

Mohammad Abu Sayem Karal

Md. Masum Billah serves as an Assistant Professor in the Department of Physics at Jashore University of Science and Technology, Bangladesh. He earned his PhD from Shizuoka University, Japan, with a specialization in membrane biophysics. His research interest is to examine the physicochemical properties of vesicles/cells and to reveal the effect of osmotic pressure and lipid compositions on the antimicrobial peptides-induced pore formation and pore evolution in model membranes, and their mechanisms.

Md. Masum Billah

coating, they have varying characteristics and levels of toxicity.[24] The substantial ratio of surface area to volume of MNPs induces aggregation to minimize surface energies.[25] Moreover, the inherent high chemical reactivity and subsequent oxidation of uncoated MNPs necessitate strategies for their structural and property preservation, commonly achieved through coating with the organic/inorganic molecules. This coating not only enhances stability but also facilitates functionalization of the MNPs.[26–30] The type of coating also affects their interactions with cell membranes.[31]

Recently, researchers have focussed on studying the giant unilamellar vesicles (GUVs) as a model of cells in various experiments.[32–35] Vesicle deformation and membrane poration are two vital processes that result from interactions between MNPs and biomembranes/lipid bilayers.[36,37] The interaction with anionic MNPs provides insights into membrane perme-ability, fluidity, and mechanism of interaction.[38,39] Studies on their interaction with GUVs help in enhancing drug delivery.[40] MNPs used in magnetic hyperthermia can be optimized by studying their interactions with GUVs.[7] In diagnostic and imaging applications, MNPs can enhance the sensitivity and specificity of biosensors,[41] improve the contrast in MRI, and their interaction with GUVs is essential for improving imaging contrast and biocompatibility.[42] In toxicological studies, devel-oping biocompatible NPs involves understanding their inter-action with GUVs.[43]

Comprehending the mechanism of interactions between MNPs and vesicles membranes is pivotal for ensuring their safe and efficient utilization in medicine.[44,45] Until now, there has been a lack of comprehensive review devoted to investi-gate the impacts of MNPs on vesicle deformation and membrane damage (poration or rupture) under various experimental conditions. We discussed the interaction of MNPs with cell mimetic GUVs under various membrane charges, buffer salt concentrations, sugar concentrations, membrane cholesterols, polymer-grafted phospholipids, and membrane potentials. These conditions greatly influence the membrane bending rigidity.[46–49] We discussed several parameters, *e.g.*, compactness, fraction of deformation and poration, dynamics of membrane permeation, and the kinetics of permeation.

2. Experimental techniques for preparing vesicles and NPs

Natural swelling is a popular approach for preparing the GUVs (size 1 μm to 100 μm)[50] by varying membrane surface charge and buffer salt concentration,[51] sugar concentration,[52] polymer grafted phospholipid,[53] and membrane potential.[54] Purification is essential to separate the GUVs from lipid aggregates and small vesicles.[55,56] The extrusion method is also a well-known technique to prepare liposomes, such as large unilamellar lipid vesicles (LUVs) of sizes 10 nm to 1 μm.[57] MNPs of size 18 nm were prepared using the green synthesis technique.[58] The zeta potential of the MNPs was -21.3 ± 4.8 mV.[51] The interac-tion of MNPs with GUVs was conducted using an inverted phase contrast fluorescence microscope. A modified oxidative hydro-lysis method was employed for coating the MNPs cores of 25–30 nm with polyethyleneimine (PEI-MNPs) and poly(acrylic acid) (PAA-MNPs).[59] The zeta potential evolution of PEI-MNPs and PAA-MNPs after incubation in DMEM supplemented with FBS showed -12 mV and -11 mV, respectively. The *in vitro* experiments on PEI-MNPs and PAA-MNPs uptake were carried out on human neuroblastoma cell line (SH-SY5Y).

3. Findings and interpretations

3.1 Effect of surface charge and salt concentration

3.1.1 Deformation and compactness of a GUV induced by MNPs. At first, the deformation of a 'single GUV' induced by MNPs is discussed by varying the membrane surface charge density and aqueous NaCl concentration. In the absence of 3.33 μg/mL MNPs, the DOPG/DOPC (60/40)-GUV exhibits a perfectly spherical shape (time $t = 0$ min in Fig. 1a). After inducing the MNPs into the vesicle's suspension, the shape of GUV remained the same for a while and start deformation at $t = 14$ min and the deformation increased with time (Fig. 1a). The degree of deformation was determined by measuring its compactness (C_{om}).[51,60]

$$C_{om} = \frac{P^2}{4\pi S_{cr}} \qquad (1)$$

Tawfika Nasrin received Master of Philosophy degree from Department of Physics, Bangla-desh University of Engineering and Technology, Bangladesh. Her research interest is investi-gating the statics and dynamics of lipid vesicles while interacting with nanoparticles.

Tawfika Nasrin

Md. Moniruzzaman received Master of Science degree from Department of Physics, Bangla-desh University of Engineering and Technology, Bangladesh. His research interest is revealing the mechanism of membrane permeation in lipid vesicles induced by nanoparticles under various membrane potentials.
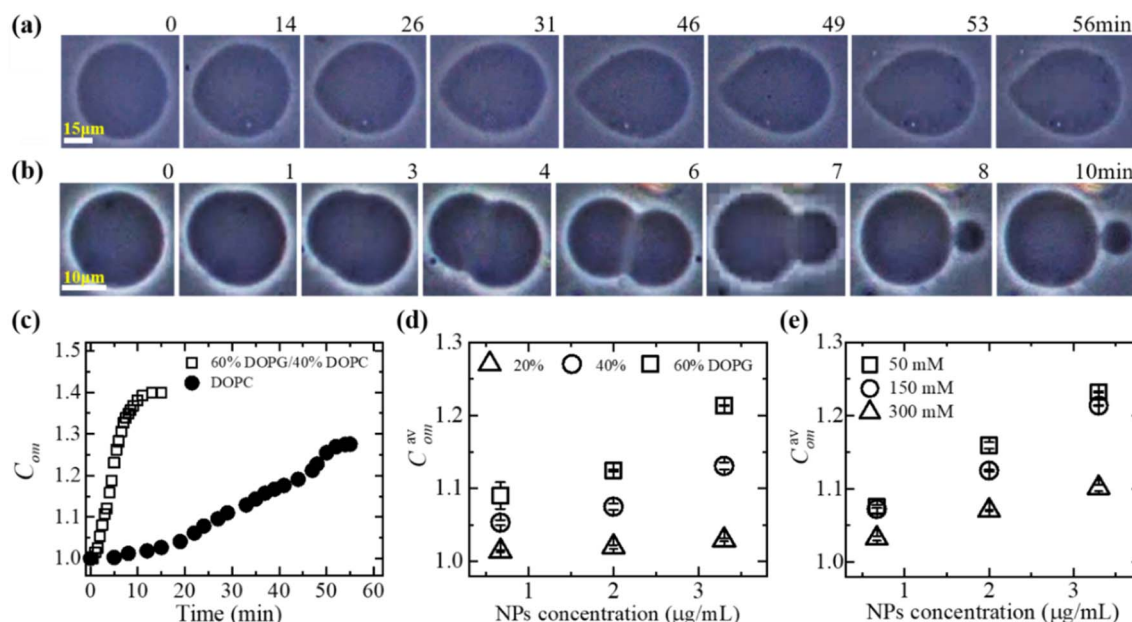
Md. Moniruzzaman

Fig. 1 Deformation of GUV and compactness. Phase contrast images shows the deformation of a (a) DOPG/DOPC (60/40)-GUV and (b) DOPC-GUV interacted with 3.33 μg/mL MNPs. The numerical values above each image represent the duration (in minutes) of MNPs adsorption. (c) Time dependent compactness (C_{om}) of the GUVs as shown in (a) and (b). (d) The MNPs concentration dependent of average compactness (C_{om}^{av}) for various DOPG%. (e) The MNPs concentration dependent of C_{om}^{av} for different NaCl concentrations. The figures have been adapted from ref. 51 with permission from Elsevier B. V., copyright 2020.

where P is the perimeter and S_{cr} is the cross-sectional area of the two-dimensional view of the vesicle. At $t = 0$ min, the $C_{om} = 1.0$ and then gradually increased to 1.274 at $t = 56$ min and remained nearly steady afterward (Fig. 1c). The similar experiment was performed for DOPC-GUVs (Fig. 1b), and hence measured the C_{om} (Fig. 1c). The average compactness (C_{om}^{av}) with ±SE increased with the increase of DOPG% (Fig. 1d), while C_{om}^{av} were greater at lower NaCl concentration (Fig. 1e) at different MNPs concentration. Thus, the deformation of GUVs is influenced by surface charge density and the buffer salt concentration.

In DOPC, hydrophilicity is maintained by a single dipole, wherein a phosphate group (PO_2^-) is separated by approximately 0.5 nm from a N^+ choline group, forming a substantial dipole denoted as ($P^- - N^+$), with a considerable magnitude of around 20 debye.[61] The orientation of the dipole vector is 50–80° concerning the normal to the bilayer surface.[62] In DOPG, hydrophilicity is achieved through multiple short dipoles formed by OH groups, each with an equilibrium bond length of 0.097 nm. The total dipole moment of a PG molecule is 1.76 debye.[63] The stronger adsorption of anionic MNPs onto DOPG/DOPC-GUVs compared to DOPC-GUVs leads to increased lateral tension in the external layer of the membrane. This elevation in tension results in greater total elastic energy and a mismatch in surface areas between the two layers (Fig. 1c). The impact of electrostatic interactions is crucial in colloidal systems and lipid vesicle suspensions.[64–67] As the surface charge density increases, the repulsive forces among lipid molecules also rise, thereby enhancing electrostatic effects.[68] On the other hand, higher salt ion in the colloidal solution acts

to shield the surface charges of membrane lipids and leads to weaker the electrostatic effect.[67,68] Thus, the electrostatic interaction effect is more pronounced at higher DOPG and lower NaCl concentrations. Consequently, higher DOPG (Fig. 1d) and lower NaCl concentration (Fig. 1e) correspond to higher C_{om} values. Additionally, increased MNPs concentrations induce greater membrane tension, further enhancing compactness.

3.1.2 Fraction of vesicle deformation induced by MNPs. Considering the electrostatic effect,[64,67,69–71] the fraction of deformation (Fr_d) of GUVs is discussed under various membrane charge density and NaCl concentration. Fr_d is defined as the ratio of number of deformed GUVs to the total number of examined GUVs. Fr_d increases with time for different DOPG% and NaCl induced by 3.33 μg/mL MNPs (Fig. 2a and c). The higher surface charge density deformed more the GUVs (Fig. 2b). In contrast, Fr_d is higher for lower salt concentration (Fig. 2d).

The formation of vesicles can result in various stationary forms with different shapes, each associated with its specific energy.[72,73] The perfectly spherical shaped GUV is characterized by a minimum free energy (E_s) compared to other stable forms. Nevertheless, there is invariably a finite chance for a GUV to maintain a stable non-spherical, or deformed, configuration, characterized by an energy (E_d) considerably exceeding that of the preferred spherical shape (E_s). Under normal situation, the probability of a vesicle adopting a spherical shape is almost one (100%), while the probability of non-spherical shaped GUV is nearly zero. The fraction of deformed GUVs can be assessed accordingly.[51]
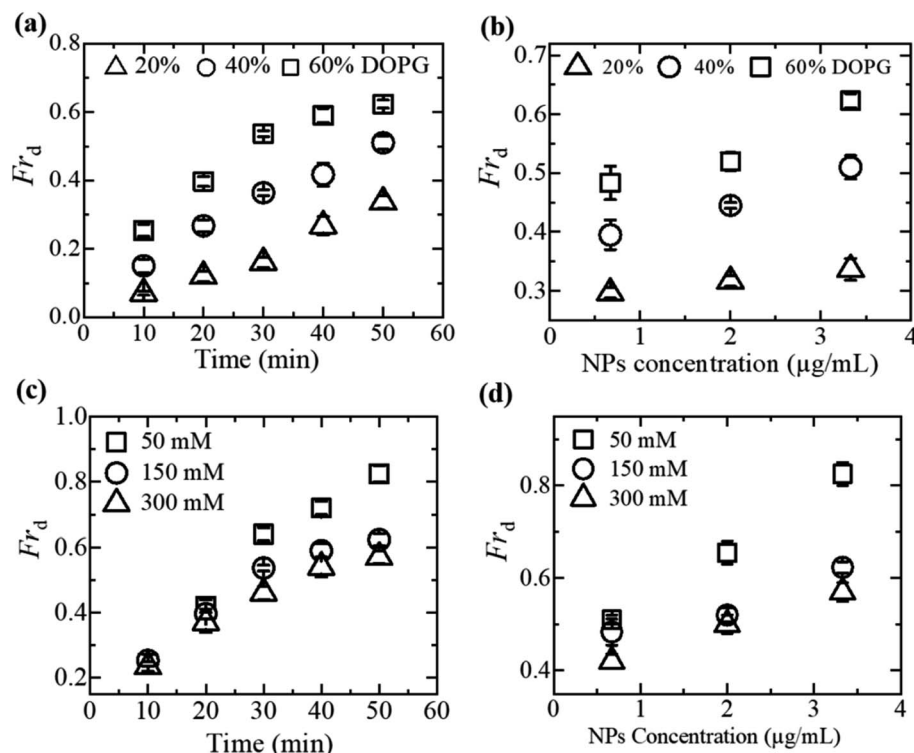
Fig. 2 Influence of membrane surface charge density and NaCl concentration on MNPs–induced fraction of deformation (Fr_d) of DOPG/DOPC-GUVs. (a) Time course of Fr_d induced by 3.33 μg/mL MNPs at various DOPG%. (b) Dependence of Fr_d on MNPs concentration for several DOPG%. (c) Time course of Fr_d induced by 3.33 μg/mL MNPs for different NaCl concentrations. (d) Dependence of Fr_d on the concentration of MNPs for various concentration of NaCl. The figures have been adapted from ref. 51 with permission from Elsevier B. V., copyright 2020.

$$Fr_d \propto \frac{1}{E_d - E_s} \approx \frac{1}{E_d}\left(1 + \frac{E_s}{E_d}\right) \quad (2)$$

The increases of E_s due the adsorption of MNPs increase the possibility of getting non-spherical GUVs. The transition rate from a spherical to a non-spherical shape is maintained by the height of the barrier energy. As the energy of E_s increases, the height of barrier energy decreases, resulting to increase the rate of transformation of spherical shaped vesicles to non-spherical ones.

3.2 Impact of sugar concentration

3.2.1 Membrane permeation induced by MNPs. Sugar's impact on membrane properties extends beyond cellular regulation,[74–76] with widespread medical and industrial applications.[77,78] Its influence spans from altering the spontaneous curvature of vesicles[79] to modulating membrane-specific capacitance,[80] bending rigidity, and susceptibility to electroporation.[81–84] The leakage of calcein (calcein has the Stokes–Einstein radius of 0.74 nm)[85,86] from the lumen of DOPG/DOPC (40/60) and DOPC-GUVs due to 3.33 μg/mL MNPs under various concentrations of sugar has been discussed (Fig. 3). At a sugar concentration of 50 mM, prior to interaction with MNPs (at time $t = 0$), phase contrast microscopy displayed two GUVs in Fig. 3a(i) and b(i), while fluorescence microscopy captured the same GUVs shown in Fig. 3a(ii) and b(ii). The

internal fluorescence intensity (FI) remained relatively constant, with minimal decay attributed to photo-bleaching, until 39 s (Fig. 3a(ii)) and 31 s (Fig. 3b(ii)), after which the GUVs became indistinguishable from the background due to a rapid decrease in luminal intensity. Following complete calcein leakage, phase contrast images revealed spherical GUV shapes without detectable breaks, as depicted in Fig. 3a(iii) and b(iii).

The time dependent FI of these representative GUVs are presented in Fig. 3(c) and (e), respectively. The decrease in FI of the GUV-lumen is attributed to the leakage of calcein molecules from the interior to the exterior of the GUVs. Consequently, upon interaction with MNPs, two distinct states of GUVs emerge: an intact state where luminal fluorescence remains unchanged, and a pore state characterized by the decrease in FI over time until reaching zero. Fig. 3(d) and (f) display the time dependent FI for several such GUVs, demonstrating that pore formation occurs at different times, indicating a stochastic process. Before starting the calcein leakage, MNPs initially bind to vesicles, inducing surface pressure on the membrane and subsequently leading to transmembrane pore. The stochastic formation of pore in several GUVs arises from the stochastic initiation of prepore in the membranes.[87–89] The average time of poration increases with rising sugar concentrations for both GUV types (Fig. 3g).

3.2.2 Compactness and fraction of deformation. Fig. 4(a) presents the average compactness (C_{om}^{av}) of DOPG/DOPC (40/60) and DOPC-GUVs interacted with 3.33 μg/mL MNPs at different
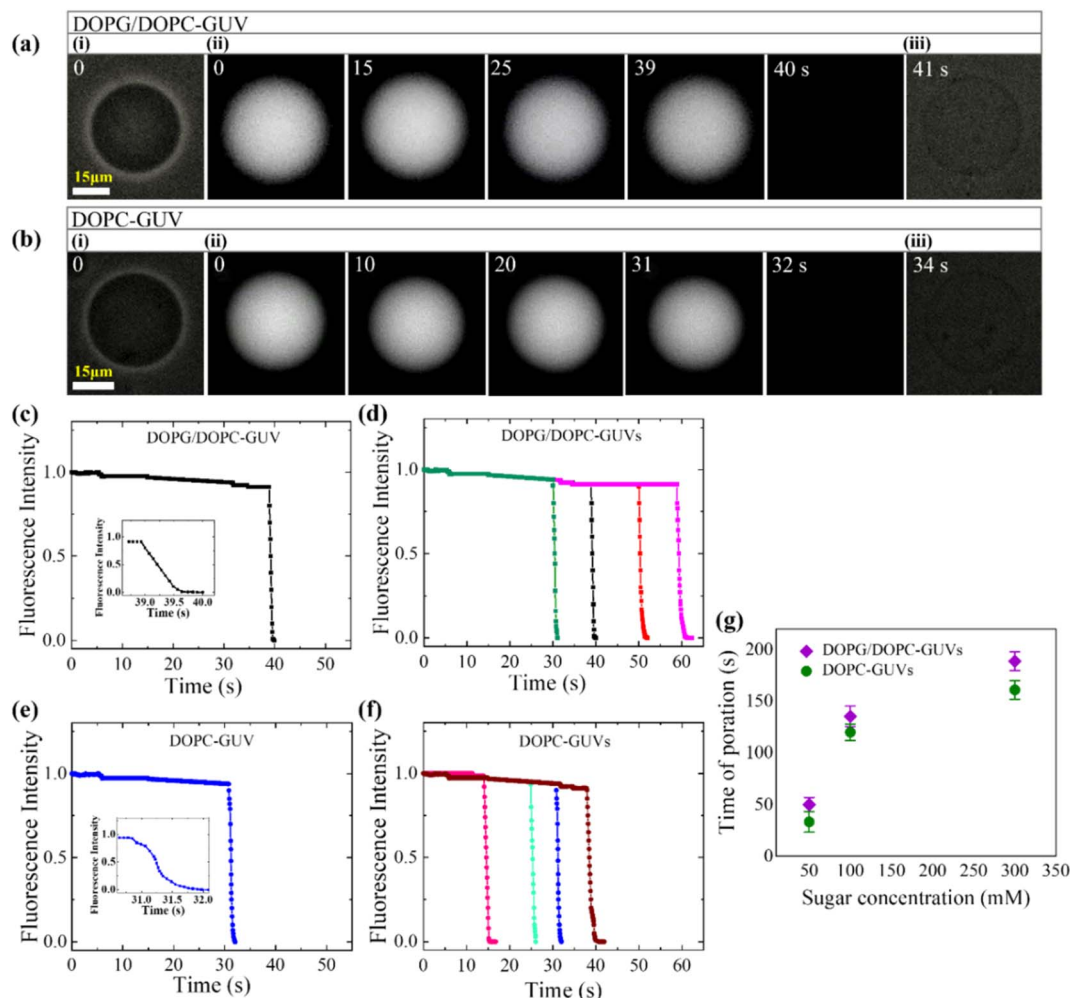
Fig. 3 The impact of sugar concentration on the calcein leakage from the interior of GUVs interacted with 3.33 μg/mL MNPs. a(i and iii) and b(i and iii) display the phase contrast images of DOPG/DOPC (40/60)-GUVs and DOPC-GUVs, respectively. The fluorescence images of the corresponding GUVs reveal a gradual reduction in calcein from the interior of the GUVs. The numbers on each image indicates the time (in second) after inducing the MNPs into the suspension of GUVs. Time dependent fluorescence intensity (FI) of calcein for (c) DOPG/DOPC (40/60)-GUVs and (e) DOPC-GUVs as displayed in (a) and (b), respectively. The inset displays the quick shift of FI over time. Time course of FI for several (d) DOPG/DOPC (40/60)-GUVs and (f) DOPC-GUVs under same condition. (g) The average time of poration varies in accordance with the concentration of sugar. The figures have been adapted from ref. 52 with permission from PLOS, copyright 2022.

sugar concentrations. C_{om}^{av} decreased with rising sugar concentration. Fig. 4b presents a comparison between the charged and neutral GUVs in terms of Fr_d and the fraction of poration (Fr_p). Fr_p is defined as the ratio of number of pored GUVs to the total number of examined GUVs. Both Fr_d and Fr_p exhibit a decrease with increasing sugar concentration. Charged GUVs demonstrate higher Fr_d compared to neutral GUVs, whereas the opposite trend is observed for Fr_p.

The bending rigidity of lipid membranes is influenced by the concentration of sugar.[81,83] At relatively low sugar concentrations, sugar molecules interact strongly with the lipid membranes, positioning themselves between the head groups of phospholipids.[90] This interaction reduces the area of the lipid head groups by increasing the surface pressure. In the aqueous phase, some of the carbohydrate molecules integrate into the membrane, acting as an additive.[79,91] The interaction between sugar and lipid head groups at lower sugar concentrations is

ascribed to enthalpy-driven forces, fostering an attractive interaction. Conversely, at higher sugar concentration, the repulsion between sugar and head group of lipids is attributed to entropy-driven forces. This interplay of attractive and repulsive interactions between sugar and lipid molecules aligns with findings from previous studies.[92,93] Under a specific concentration of MNPs, surface pressure is lesser at higher sugar concentrations compared to lower ones, owing to the differing amount of bound sugar molecules at the bilayer interface. These variations in surface pressure significantly impact the membrane stability, compactness as well as deformation.

3.3 Cholesterol effect

3.3.1 Encapsulating calcein leakage induced by MNPs. Lipids and cholesterol are fundamental constituents of cell membranes.[94] Fig. 5 presents an experimental finding due to the interaction of 3.33 μg/mL MNPs with DOPG/DOPC/Chol (46/
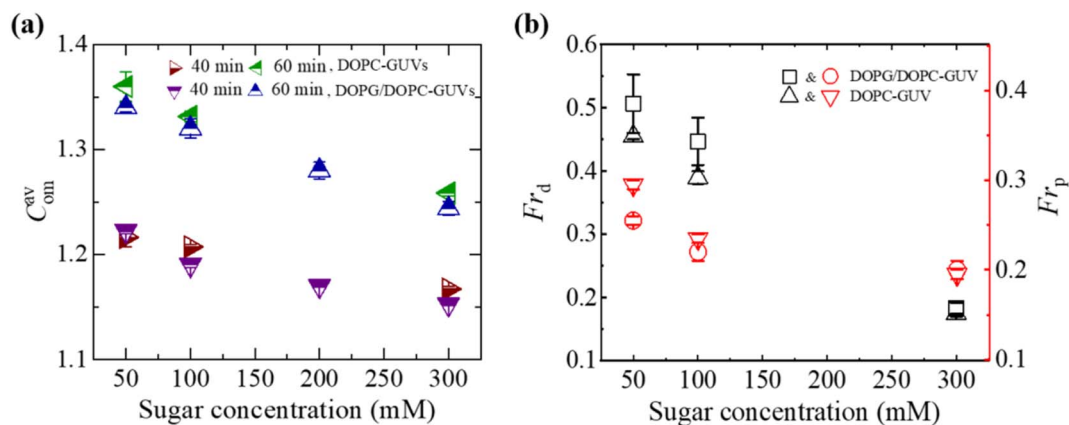
Fig. 4 Sugar concentration dependent C_{om}^{av}, Fr_d, and Fr_p in DOPG/DOPC (40/60)-GUVs and DOPC-GUVs interacted with 3.33 μg/mL MNPs. (a) Sugar concentration dependent C_{om}^{av} at 40 and 60 min. (b) Sugar concentration dependent Fr_d and Fr_p at 40 min. The figures have been adapted from ref. 52 with permission from PLOS, copyright 2022.

39/15)-GUVs. Prior to MNPs interaction, Fig. 5a(i) displays the phase contrast image of the GUV, while Fig. 5a(ii) depicts the same GUV under fluorescence microscopy, exhibiting high lumen intensity attributed to calcein presence within the GUV. As seen in Fig. 5a(ii), the fluorescence intensity (FI) remained constant for 40 s after adding MNPs. Then the FI decreased gradually for a while. The intensity dropped off significantly between 40 s and 65 s, and it quickly dropped to zero at 68 s. Upon the completion of calcein leakage, the same GUV was revealed with unchanged size and shape in the phase-contrast microscopy (Fig. 5a(iii)). The permeation of calcein occurs through the nanopore.[95] The vesicle lumen intensity with time is presented in Fig. 5b.

The stochastic nature of pore formation reveals variations in poration timing among multiple GUVs (Fig. 5c). The average poration time increases with higher cholesterol (Fig. 5d). In addition, the average poration time for DOPG/DOPC/Chol-GUVs is much greater than that of DOPC/Chol-GUVs. Thus, the incorporation of cholesterol into membranes suppresses MNPs-induced poration.

3.3.2 Compactness, fraction of deformation, and poration. Fig. 6a displays the time dependent increase in C_{om}^{av} of DOPG/DOPC/Chol-GUVs induced by 3.33 μg/mL MNPs. The C_{om}^{av} decreased with the rise of cholesterol for both charged DOPG/DOPC/Chol-GUVs and neutral DOPC-GUVs (Fig. 6b). Both the Fr_d and Fr_p decrease with increasing cholesterol
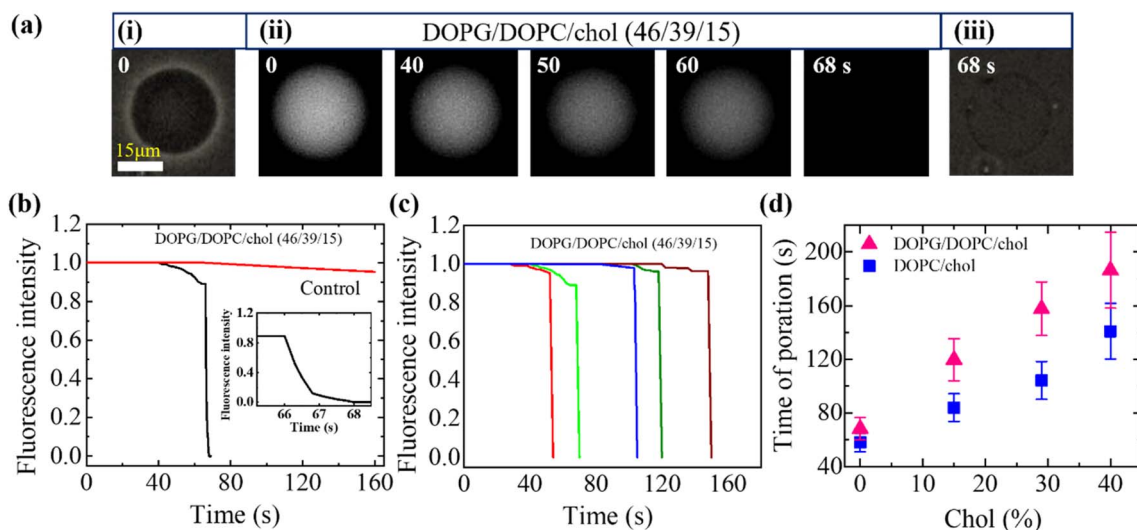

Fig. 5 Calcein leakage from the interior of DOPG/DOPC/Chol-GUVs interacted with 3.33 μg/mL MNPs. (a) Phase contrast fluorescent microscopic images of the DOPG/DOPC/Chol (46/39/15)-GUVs. (i) and (iii) show the phase contrast image, and (ii) shows the fluorescence images of the gradual change in encapsulating calcein. The numerical values on each image represent the duration (in seconds) of MNPs introducing into the suspension of GUVs. (b) Time dependent fluorescence intensity (FI) of GUV as shown in (a). The inset displays the quick shift in FI over time. (c) Time dependent FI for five separate GUVs as the same conditions of (b). (d) Cholesterol dependent pore formation time (with SD). The figures have been adapted from ref. 95 with permission from Royal Society of Chemistry, copyright 2022.
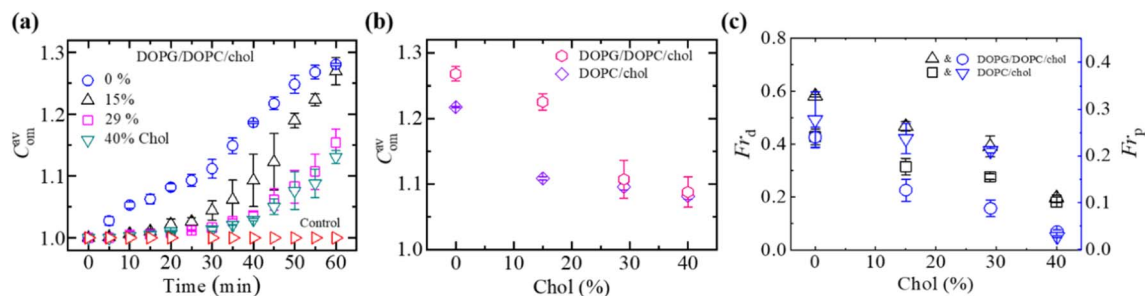
Fig. 6 The C_{om}^{av}, Fr_d, and Fr_p of DOPG/DOPC/Chol-GUVs induced by 3.33 µg/mL MNPs. (a) Time course of C_{om}^{av} for various cholesterol contents. (b) Cholesterol dependent C_{om}^{av} of charged and neutral GUVs at 50 min. (c) Cholesterol dependent Fr_d and Fr_p at 50 min. The figures have been adapted from ref. 95 with permission from Royal Society of Chemistry, copyright 2022.

(Fig. 6c). The Fr_d for DOPG/DOPC/Chol was higher compared to DOPC/Chol-GUVs. As the bilayer bending rigidity increases with cholesterol,[49] hence presence of cholesterol content decreases the poration along with deformation.

3.4 Effect of polyethylene glycol (PEG)-grafted phospholipid

3.4.1 Vesicle compactness induced by MNPs. Polyethylene glycol (PEG)-grafted phospholipids are recognized for their significant contribution to membrane stability through various mechanisms, including increasing lateral membrane-tension, enhancement of membrane hydrophilicity, and modulation of mechanical properties such as the bending rigidity.[96–98] To observe the effects of PEG-grafted 1,2-dioleoyl-sn-glycero-3-phospho ethanolamine-N-[methoxy(polyethylene glycol)-2000] (e.g., PEG-DOPE) on the deformation, the interaction of 2.00 µg/mL MNPs with the PEG-DOPE/DOPC-GUVs has been discussed. Fig. 7a shows the time dependent C_{om}^{av} in which C_{om}^{av} is higher for PEG-DOPE/DOPC (5/95)-GUVs and lower for PEG-DOPE/DOPC (0/100)-GUVs. Fig. 7b shows the linear increase in C_{om}^{av} on the PEG-DOPE% at different time of interaction. The large PEG polymer connected to the DOPE headgroup increases the deformation induced by MNPs. This is due to the development of large entropy in the membrane–water interface, attributed to the extended chain of PEG polymer in the head-

groups of PEG-DOPE, which continually disrupts the stability of the lipid membrane.[52]

3.4.2 Leakage of encapsulating calcein. The study examined the interaction between 2.00 µg/mL MNPs and PEG-DOPE/DOPC-GUVs as depicted in Fig. 8. The reduction in fluorescent intensity (FI) of the GUV-lumen signifies the leakage of encapsulated calcein, as shown in Fig. 8a. Fig. 8b displays the time dependent FI, revealing the initiation time of pore formation in the membrane observed in Fig. 8a. Furthermore, Fig. 8c presents the FI of multiple GUVs, highlighting the stochastic pore formation. Fig. 8d indicates that with the increase of PEG-DOPE%, the average time of pore formation (t_{ave}) decreased (i.e., poration required shorter time). Finally, Fr_d and Fr_p have been compared for various PEG-DOPE in Fig. 8e. The presence of higher PEG-DOPE in the membrane accelerates MNPs-induced deformation of GUVs. The Fr_p also increases with the increase of PEG-DOPE, however, the rate of increment of Fr_p is higher than that of Fr_d. In the scenario involving PEG-DOPE/DOPC-GUVs, two distinct interaction effects come into play: electrostatic attraction between MNPs and N^+ (whereas repulsion occurs between MNPs and P^-), and the intra-membrane electrostatic effect attributable to PEG-DOPE, with DOPE serving as a negatively charged lipid. The adsorption of MNPs onto the outer layer triggers the stretching in the membrane,
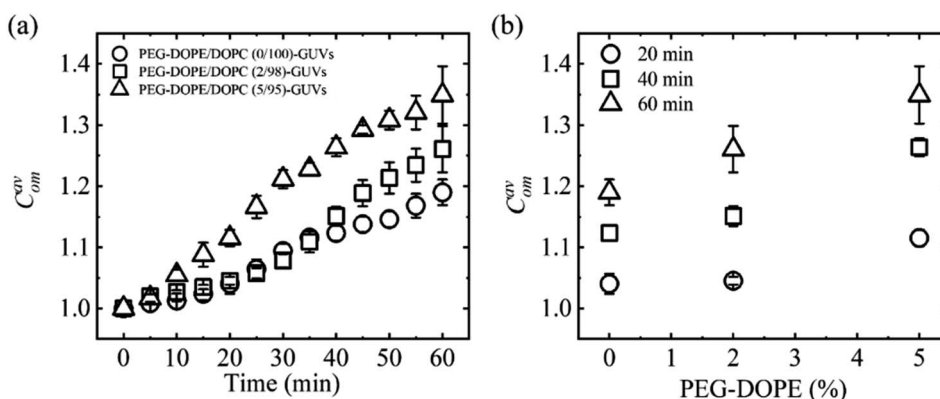

Fig. 7 Compactness of PEG-DOPE/DOPC-GUVs interacted with 2.00 µg/mL MNPs. (a) Time course of C_{om}^{av} under various PEG-DOPE%. (b) PEG-DOPE% dependent C_{om}^{av} at several times. The figures have been adapted from ref. 53 with permission from PLOS, copyright 2023.
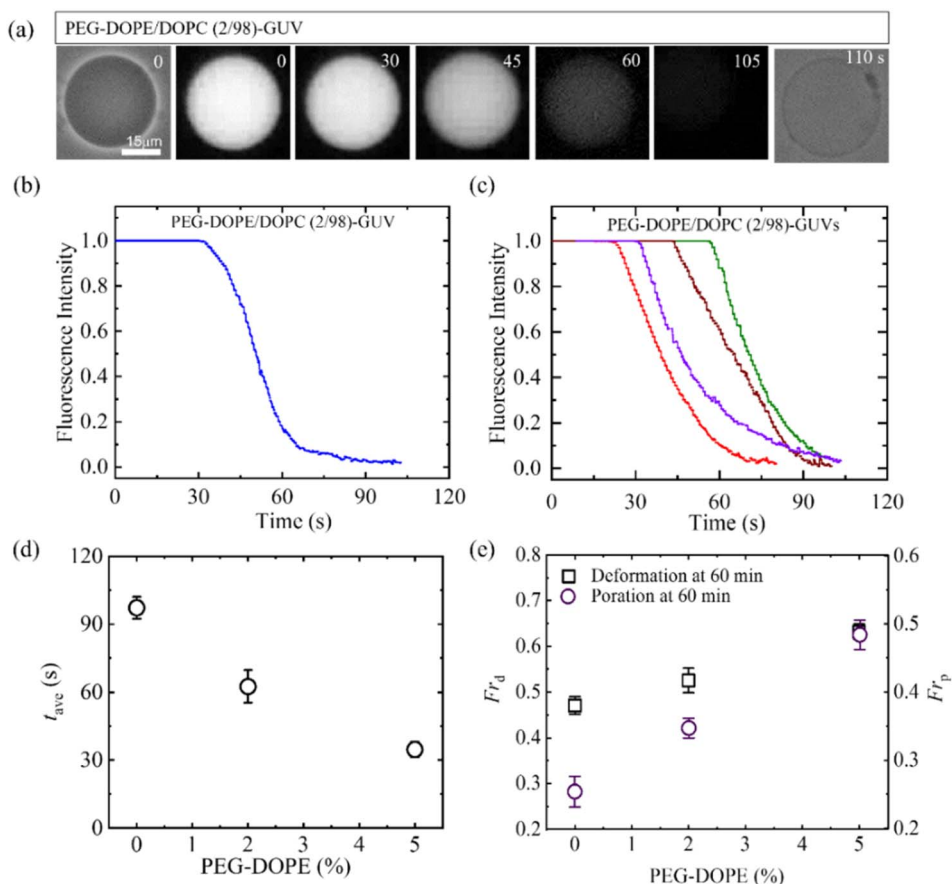
Fig. 8 Effects of PEG-DOPE on the calcein leakage from the interior of GUVs interacted with 2.00 μg/mL MNPs. (a) PEG-DOPE/DOPC (2/98)-GUV in the phase contrast and fluorescence images before and after the interaction of MNPs. The time in second indicates the time of interaction of MNPs with GUVs. (b) Time dependent fluorescence intensity (FI) as displayed in (a). (c) Time dependent FI for several GUVs under the same conditions of (b). (d) PEG-DOPE% dependent average poration time in GUVs. (e) PEG-DOPE% dependent Fr_d and Fr_p at 60 min of interaction of MNPs. The figures have been adapted from ref. 53 with permission from PLOS, copyright 2023.

ultimately leading to pore formation. This mechanism is similar to the pore formation induced by antimicrobial peptides.[88]

3.5 Effect of membrane potential

3.5.1 Membrane permeation and leakage constant. Living organisms typically uphold a negative membrane potential (φ_m) spanning from −20 to −120 mV,[99] a phenomenon attributed to ion diffusion through ion channels connecting the interior and exterior aqueous medium of cells.[100] This membrane potential is crucial for various cellular functions, including membrane permeability, cell proliferation and division, protein localization, and binding.[101–105] Furthermore, it significantly impacts the efficacy of ion transport, secretion, metabolism, and homeostasis.[106] The value of φ_m was determined using the Nernst equation,[107,108]

$$\varphi_m = \frac{RT}{F} \ln \frac{[K^+]_{out}}{[K^+]_{in}} = 25.7 \ln \frac{[K^+]_{out}}{[K^+]_{in}} [mV] \qquad (3)$$

In this equation, R represents the molar gas constant, T denotes the absolute temperature, and F represents the Faraday constant. The $[K^+]_{out}$ and $[K^+]_{in}$ indicate the respective concentrations of K^+ outside and inside the GUVs.

To discuss the effects of φ_m, at first, 2.00 μg/mL MNPs interacted with DOPG/DOPC/GrA (40/60/0.01)-GUVs under $\varphi_m = 0$. Utilizing GrA (*i.e.*, Gramicidin A) primarily aims to establish ion channels in the lipid bilayer, as studies earlier.[109–111] These ion channels are effective in generating a membrane potential across the bilayer, thereby contributing to crucial cellular processes.[104,112] Fig. 9a(i) shows the phase contrast image of the GUV before addition of MNPs. After adding the MNPs, the fluorescence of the GUV-lumen remained same for a while as shown in Fig. 9a(ii). The lumen intensity started decreasing gradually and at a certain stage, the GUV-lumen was indistinguishable from the background. The phase contrast image at 240 s of the same GUV shown in Fig. 9a(iii). Fig. 9b shows the time dependent leakage of fluorescence intensity (FI) as presented in Fig. 9a. The FI of GUV-lumen is shown to remain nearly constant until 68 s, and ~90% calcein leaked out in 180 s. Fig. 9c shows the time dependent leakage of several GUVs, in which the leakage happens at different times. Subsequently, the impact of 2.00 μg per mL MNPs on DOPG/
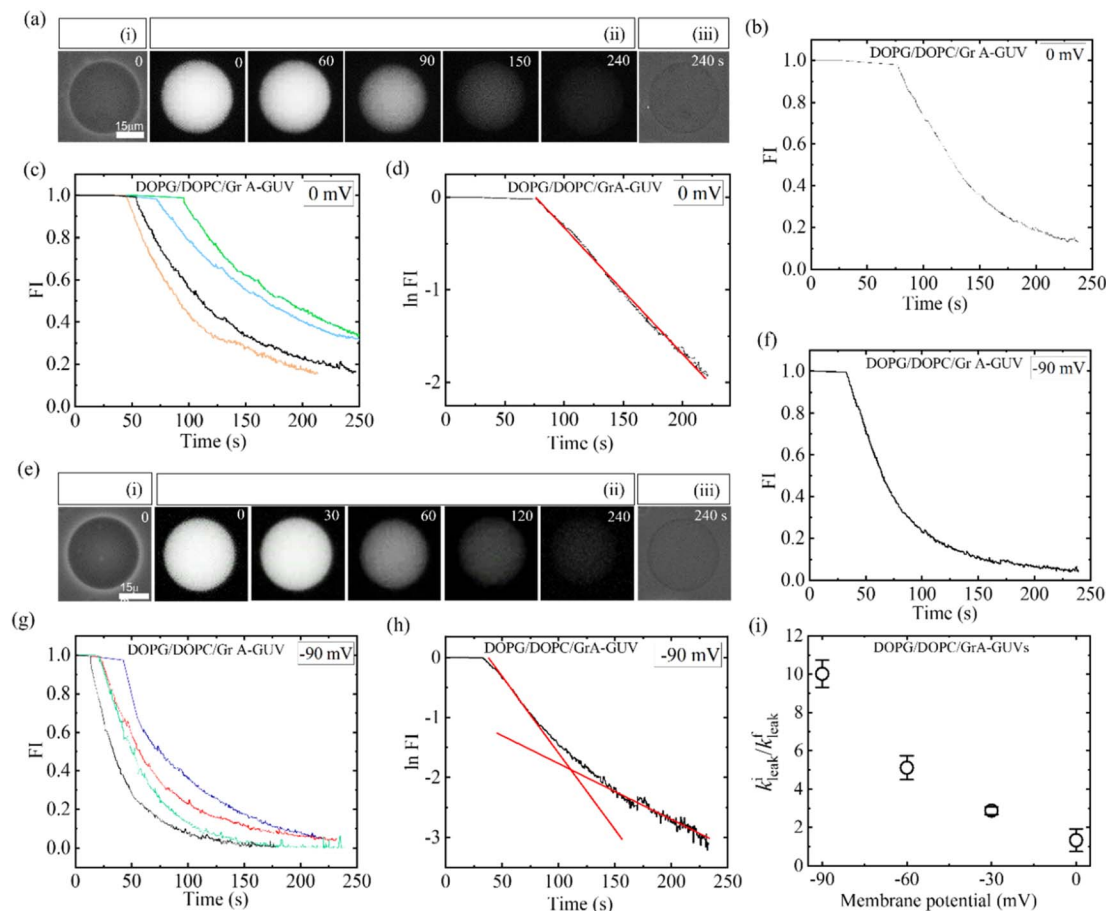
Fig. 9 DOPG/DOPC/GrA (40/60/0.01)-GUVs under $\varphi_m = 0$ and $\varphi_m = -90$ mV interacted with 2.00 μg/mL MNPs. (a) Calcein leakage from the inside of GUV under $\varphi_m = 0$. Phase contrast images before and after the interaction of MNPs are shown in (i) and (iii), respectively. (ii) Fluorescence images of the GUV after the introduction of MNPs. (b) Time dependent fluorescence intensity (FI) as shown in (a). (c) Time dependent FI for several GUVs under the identical condition of (b). (d) Time dependent logarithm of FI under $\varphi_m = 0$, where the fitting curve of eqn (4) is represented by a solid red line. (e) Calcein leakage from the inside of GUV under $\varphi_m = -90$ mV. Phase contrast images captured both before and after the introduction of MNPs are shown in (i) and (iii), respectively. (ii) The fluorescence images of the same GUV following the interaction of MNPs. (f) Time dependent FI for several GUVs under the identical condition of (e). (g) Time dependent FI for several GUVs under the same condition of (f). The time of interaction, depicted in seconds, is annotated on each fluorescence image in panels (a) and (e). (h) Time dependent logarithm of FI at $\varphi_m = -90$ mV, where the solid line (red) shows the fitting curve of eqn (4). (i) Membrane potential dependent k_{leak}^i/k_{leak}^f. The figures have been adapted from ref. 54 with permission from Royal Society of Chemistry, copyright 2023.

DOPC/GrA (40/60/0.01)-GUVs is examined under $\varphi_m = -90$ mV, contrasting with observations made at $\varphi_m = 0$ mV. Fig. 9e presents microscopic images of a single GUV at $\varphi_m = -90$ mV, showing the phase contrast image prior to MNPs addition (Fig. 9e(i)), fluorescence images captured at various interaction timepoints (Fig. 9e(ii)), and the phase contrast image at 240 s post-interaction (Fig. 9e(iii)). Additionally, Fig. 9f presents the time dependent FI observed in Fig. 9e.

This indicates, until 35 s, the FI remains constant, and then gradually dropped to zero at 240 s. The same leakage pattern is observed for several GUVs under the same condition (Fig. 9g). At $\varphi_m = -90$ mV, 60% GUVs experienced pores, but at $\varphi_m = 0$, it was 30%. At $\varphi_m = 0$ mV, the leakage exhibits a decay pattern consistent with a single exponential function (Fig. 9d), contrasting with the absence of such decay pattern observed at $\varphi_m = -90$ mV (Fig. 9h). To obtain the leakage rate constant (k_{leak}),

the time course of logarithmic FI was fitted at initial state and final state separately using an equation as follows:

$$\ln[FI^{in}(t)/FI^{in}(t_0)] = -k_{leak}(t - t_0) \qquad (4)$$

where $FI^{in}(t_0)$ is the initial lumen intensity (*i.e.*, lumen intensity at $t = t_0$), $FI^{in}(t)$ is the lumen intensity at any other time t, and t_0 is the onset time of decrease in FI (*i.e.*, the onset time of leakage of GUV's internal contents). In some cases, two rate constants of leakage, termed as k_{leak}^i and k_{leak}^f are considered as the rate of initial stage leakage and final stage leakage, respectively.

At $\varphi_m = 0$ mV, the leakage constant (k_{leak}) for several GUVs was obtained $(9.20 \pm 0.09) \times 10^{-3}$ s^{-1}. For $\varphi_m = -90$ mV, both the initial and final stages were fitted using eqn (4), and obtained two rate constants, namely initial leakage constant k_{leak}^i and final leakage constant k_{leak}^f. The corresponding values
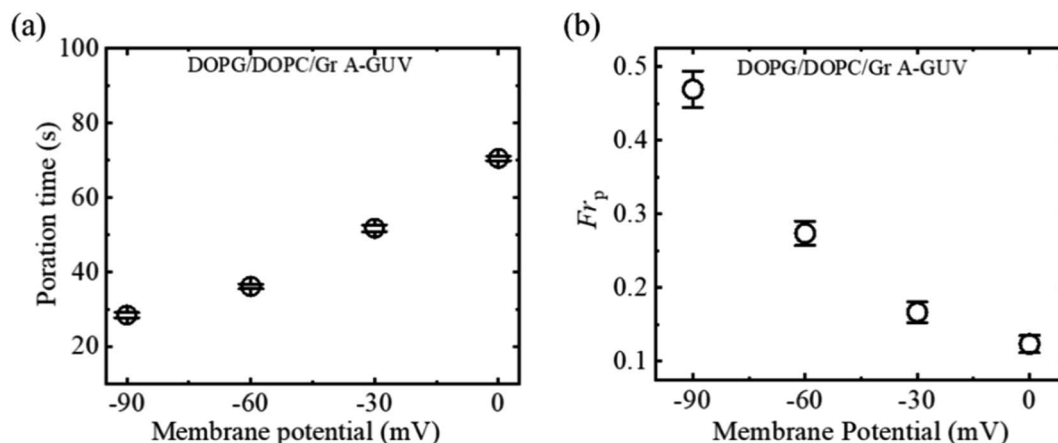
Fig. 10 Membrane potential dependent (a) Fr_p and (b) Fr_d of DOPG/DOPC/GrA (40/60/0.01)-GUVs due to the interaction of 2.00 µg/mL MNPs. The figures have been adapted from ref. 54 with permission from Royal Society of Chemistry, copyright 2023.

of k^i_{leak} and k^f_{leak} for several experimented GUVs were obtained $(23.02 \pm 0.09) \times 10^{-3} \text{ s}^{-1}$ and $(1.96 \pm 0.02) \times 10^{-3} \text{ s}^{-1}$. The k^i_{leak}/k^f_{leak} rises with the negative membrane potential (Fig. 9i). Consequently, the rate of leakage at the beginning stage increased more quickly and the rate of leakage at the end stage decreased more slowly as the φ_m increased. The similar calcein leakage is also observed for the antimicrobial peptide.[113]

3.5.2 Fraction of poration and deformation. The fraction of poration (Fr_p) and fraction of deformation (Fr_d) of DOPG/DOPC/GrA (40/60/0.01)-GUVs induced by 2.00 µg/mL MNPs for different φ_m have been investigated. Fig. 10a shows the Fr_p increases with the increase in φ_m. On the other hand, the φ_m dependent Fr_d indicates that the GUVs only exhibited deformation when there was no membrane potential (Fig. 10b).

The absence of GrA in DOPG/DOPC (40/60)-GUVs results in a rapid leakage phenomenon (shown in Fig. 3), where the logarithm FI follows a linear trend. The rapid leakage is attributed to the creation of submicron pores in the membrane.[87,114] Adding GrA significantly alters the membrane's surface tension.[110] Furthermore, GrA impacts the spontaneous curvature of the monolayer,[111] leading to changes in the mechanical characteristics of the bilayer. This alteration results in a slower leakage of calcein from the DOPG/DOPC/GrA (40/60/0.01)-GUVs due to the adsorption of MNPs (Fig. 9c). Under higher φ_m, a considerable number of MNPs become adsorbed to the outer layer of the bilayer, consequently increasing tension in the external layer. In the early stages of leakage, a larger single pore forms as a result of increased surface pressure caused by the enhanced tension. At the first stage of poration, a rapid leakage is seen because the larger pore causes a greater rate of calcein leakage. After initiation of leakage, the pore size becomes smaller, resulting a slow leakage at final stage.[54] When a membrane potential is present, it induces elevated external tension on the vesicle membrane, exceeding the energy threshold required for deformation. Consequently, under higher membrane potential conditions, vesicles are more prone to undergo poration rather than deformation.

4. Interaction of anionic polystyrene NPs with liposomes

In this section, we discuss the interaction of anionic NPs with liposomes (size 10 nm to 1 µm) instead of GUVs (size 1–100 µm). The carboxyl-modified (≈ 0.91 e$^-$ nm^{-2}) anionic white polystyrene nanoparticles (PNPs) latex of size 20 nm were mixed by vortex into the DLPC liposome containing embedded Laurdan, which is an uncharged fluorescent dye whose emission indicates the phase state of phospholipid membranes (Fig. 11).[115] The local phase state of lipid bilayer can be altered by the binding of anionic PNPs, which preferentially interact with the N-terminus of the PC head group. This interaction increases the tilt angle from 0° to 3°, characteristic of the fluid phase (Fig. 11a and b). The deformation of vesicles can be well explained by the analysis of changing the dipole angle. In Fig. 11c, the progressive rise of blue emission and loss of red emission as PNPs concentration increased—suggestive of fluid–gel phase coexistence such that the proportion of fluid to gel phase varies. Fig. 11d shows the intensity fraction of these two peaks plotted against the normalized concentration of PNPs, revealing that the changes are linear over a considerable range of PNP concentrations. The findings are independent of the lipid choice. The interaction between anionic PNPs and liposomes was confirmed by the shrinking of liposomes, as the area per lipid head group is smaller in the gel phase compared to the fluid phase.[115]

5. PEI-MNPs and PAA-MNPs uptake by SH-SY5Y

We discuss the cell viability of SH-SY5Y cell line when incubated with PEI-MNPs and PAA-MNPs at 15 and 72 h incubation time in Fig. 12.[59] The analysis, conducted using Trypan blue assays and flow cytometry, revealed that cell viability levels for both PEI-MNPs and PAA-MNPs were comparable to the control sample, even at a concentration of 50 µg/mL of MNPs. Notably,
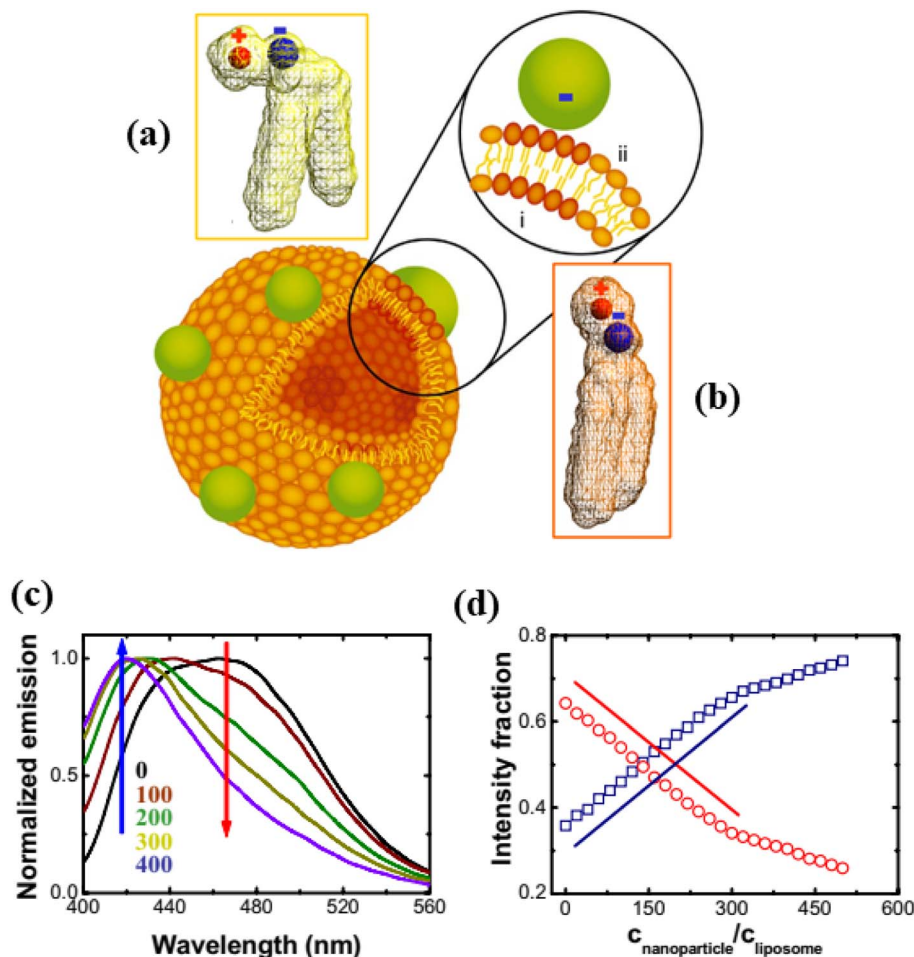
Fig. 11 Binding of anionic PNPs to the lipid bilayer. Schematic diagram of the binding-induced reorientation of the PC head group causes lipids in the fluid phase to have lower density (a) than in the gel phase (b). The fluorescence spectrum of Laurdan shows (c) normalized emission plotted against wavelength after anionic PNPs bind to 200 nm DLPC liposomes and (d) the intensity fraction of blue and red emission at 416 (blue) and 473 nm (red) is plotted against C_{NPs}/C_L. Lines with slope of unity are drawn for comparison. The figures have been adapted from ref. 115 with permission from The National Academy of Sciences of the USA, copyright 2008.
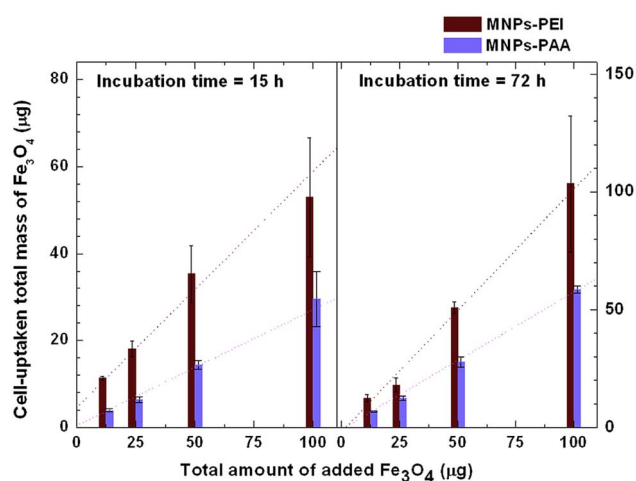

Fig. 12 Cell-uptaken total mass as a function of total added amount of PEI-MNPs and PAA-MNPs at 15 and 72 h incubation time. The figures have been adapted from ref. 59 with permission from Elsevier B. V., copyright 2014.

the amount of MNPs associated with the cells was significantly higher for PEI-MNPs than for PAA-MNPs. Consequently, the data in Fig. 12 pertains to MNPs that are either incorporated into or strongly attached to the cell membrane. A linear relationship was observed between the total amounts of added and incorporated MNPs for both types. At 15 h, the uptake rate as a function of MNP concentration was fitted with straight lines, yielding slopes of 0.54 for PEI-MNPs and 0.27 for PAA-MNPs, respectively. The cells were able to incorporate only a 54% (PEI-MNPs) and 27% (PAA-MNPs) of the particles available. At 72 h, the increase was also linear, but the slopes 1.03 for PEI-MNPs indicated that after replication the new cells were able to incorporate the 100% of the MNPs added. In contrast, for the PAA-MNPs, the slope was 0.58, meaning that only 58% of the MNPs could be incorporated. Hence different proteins adsorbed could in turn determine different cell internalization pathways. The MNPs can be completely engulfed by the cell membrane and subsequently detach from the inner surface in a process known as fission, leaving behind a typically transient membrane pore.[116,117] If the adhesion energy is not sufficiently

strong, the NPs undergo Brownian collisions with the membrane without adhering. Alternatively, the NPs can sit at the membrane interface, partially wrapped by the lipid bilayer.

6. Mechanism of deformation and poration of vesicles induced by MNPs

To consider the mechanism of MNPs-induced deformation (shape change) and poration (membrane permeation), a hypothesis has been proposed on the adsorption of MNPs into the external layer of lipid membrane as illustrated in Fig. 13. The adsorption mechanism of anionic MNPs is quite similar as discussed in Section 4. In DOPC head groups, electric dipole (*e.g.*, P^-–N^+ dipole) occurs between the choline group (N^+) and the phosphate group (P^-) (Fig. 13a). At the beginning, the bilayer-surface and the vector of dipole moment is aligned at an acute angle. Because of the electrostatic attraction that considerably alters the dipole's alignment, the adsorbed MNPs are attracted to the N^+ terminus (Fig. 13b). In accordance with the bilayer coupling model, the vesicle's spherical shape is governed primarily by the elastic energy (W_{el}), which arising from the bilayer bending energy (W_b).[49,118] It doesn't consider the monolayer stretching energy (W_r). In the ADE (area difference elasticity) model,[119,120] $W_{el} = W_b + W_r$ where $W_r \propto (\Delta A - \Delta A_0)$.[2] Here ΔA_0 denotes the area difference in the absence of MNPs and ΔA denotes the area difference in the presence of MNPs between the exterior and interior layer of the bilayer. MNPs adhering to the exterior layer induce membrane stretching, causing an area mismatch between the layers and resulting in GUV deformation. The adsorption of MNPs on the exterior layer induces a stretching, *e.g.*, lateral tension (σ) in both the layers. Such tension leads to the creation of membrane pores or vesicle rupture.[121–126] However, the direction of σ is opposite for the interior and exterior layers, as indicated by arrowheads in Fig. 13c. Consequently, thermal fluctuations of lipid molecules in the MNPs-binding region increase, leading to prominent local condensation and rarefaction of lipid molecules. This heightened local rarefaction enhances the probability of forming nanopores. The initial stage of nanopore formation can be evaluated by monitoring the decrease in fluorescence intensity from the inside of GUVs.[88,127] Nevertheless, the nanopore are unable to undergo further growth into

micrometer-scale pore due to the dominance of line tension, Γ, (*e.g.*, pore edge tension) at the pore rim, which effectively counters the lateral membrane-tension (σ) and facilitates the closure of the pore (Fig. 13d).[128–130] The prepore free energy is expressed as follows:[124,131–134]

$$E(r, \sigma) = 2\pi r \Gamma - \pi r^2 \sigma, \qquad (5)$$

where, r denotes the pore radius. The transmembrane pore formed when overcomes a threshold value (*e.g.*, energy barrier, $E_b = \pi \Gamma^2 / \sigma$). In this case toroidal pore (shown in Fig. 13d) is considered.[135,136] Thus, the deformation is explained using the ADE model, in which the MNPs are trapped at the outer layer of the membranes before poration. In the case of poration, the MNPs might diffuse to the inside of the GUVs through pores.

7. Significance of this study

The interaction of anionic NPs with giant vesicles, liposomes, and cells can significantly contribute to multiple scientific disciplines, including chemistry, physics, materials science, biology, and chemical engineering. Understanding the interaction mechanisms between anionic MNPs and GUVs aids in the synthesis of more effective MNPs with specific surface chemistries tailored for biomedical applications.[42] This can shed light on the chemical stability and reactivity of MNPs in biological environments, influencing the development of MNPs that maintain functionality under physiological conditions.[7] This also help in exploring how MNPs interact with GUVs can inform on their magnetic behavior in biological systems, essential for applications in magnetic hyperthermia and imaging.[39] This review can delve into the physics of electrostatic interactions between anionic MNPs and lipid bilayers, enhancing the understanding of fundamental principles governing NPs-membrane interactions. In materials science, the insights into the interaction between MNPs and GUVs can guide the design of nanomaterials with specific properties for targeted drug delivery and other biomedical applications.[137] In addition, understanding how MNPs interact with lipid membranes helps in developing colloidally stable formulations that are crucial for *in vivo* applications.[43] In biology, the MNPs–GUVs interaction can elucidate how NPs affect cellular membranes, which is
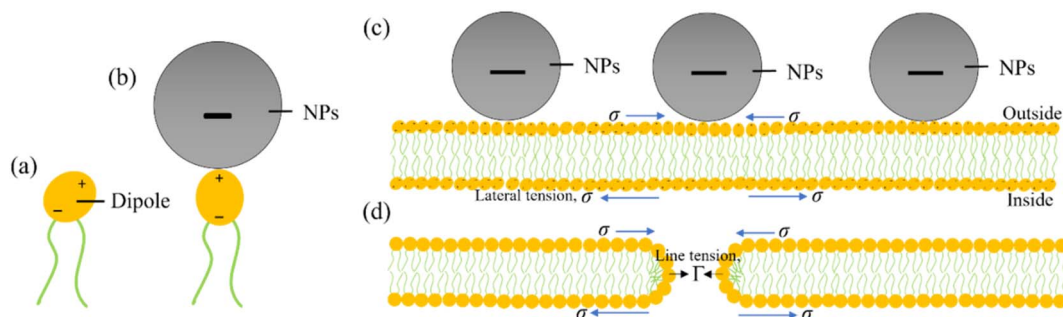

Fig. 13 An illustration on the adsorption of anionic MNPs in the membrane. (a) A DOPC molecule where lipid head acts as a dipole. (b) Adsorption of a MNPs into the DOPC lipid head. (c) Adsorption of MNPs into the lipid membrane. (d) Formation of a toroidal pore in the membrane.

critical for understanding MNPs uptake and intracellular trafficking.[138] It highlights how functionalized MNPs can be used for targeted drug delivery and diagnostic applications, enhancing the therapeutic potential of these nanomaterials. In chemical engineering, understanding the interaction mechanisms helps in optimizing the production processes for MNPs, ensuring reproducibility and scalability for industrial applications.[139] This can provide a comprehensive overview of the safety and efficacy of MNPs in biomedical applications, guiding the development of safe and effective NPs-based therapies.[40] Thus, this review on the interaction of anionic MNPs with GUVs contributes to the development of multiple scientific disciplines by providing a comprehensive understanding of the fundamental principles and practical applications of these interactions. This interdisciplinary knowledge fosters innovation in nanotechnology, enhances the development of targeted therapies, and informs the design of safer and more effective nanomaterials.

8. Concluding remarks

This review explores the influences of several elements on vesicle deformation and poration induced by anionic MNPs. The factors such as the membrane surface charge, salt and sugar concentrations in the buffer, as well as the membrane potential, can all play roles in influencing the deformation and poration of cell sized vesicles. The inclusion of membrane cholesterol and polyethylene glycol influence MNPs-induced vesicle deformation and lipid membrane poration significantly. Gramicidin A impacts the adsorption mechanism of MNPs. Taking into account the membrane potential, researchers along with clinicians have the opportunity to refine the design and optimization of MNPs, aiming to mitigate their detrimental impacts on cellular membranes and overall cellular functionality.[140] The exploration of various leakage regimes holds significant importance in evaluating the impact of MNPs on cells. Overall, this review contributes in revealing the fundamental mechanism underlying the interaction of anionic NPs with cells/vesicles, and offers crucial insights for the secure and efficient advancement of nanotechnology-based biomedical applications.

Data availability

The corresponding author is available to provide the data supporting these findings upon request, in accordance with reasonable inquiry.

Author contributions

The authors designed the paper, organizing the graphical representations and data, as well as drafting the manuscript.

Conflicts of interest

The authors affirm that there are no conflicts of interest.

References

1 G. Han, P. Ghosh and V. M. Rotello, *Nanomedicine*, 2007, **2**, 113–123.

2 W. H. D. Jong and P. J. A. Borm, *Int. J. Nanomedicine*, 2008, **3**(2), 133–149.

3 D. A. Giljohann, D. S. Seferos, W. L. Daniel, M. D. Massich, P. C. Patel and C. A. Mirkin, *Angew Chem. Int. Ed. Engl.*, 2010, **49**, 3280–3294.

4 S. Salassi, E. Canepa, R. Ferrando and G. Rossi, *RSC Adv.*, 2019, **9**, 13992–13997.

5 R. Awasthi, A. Roseblade, P. M. Hansbro, M. J. Rathbone, K. Dua and M. Bebawy, *Curr. Drug Targets*, 2018, **19**, 1696–1709.

6 S. M. Dadfar, K. Roemhild, N. I. Drude, S. von Stillfried, R. Knüchel, F. Kiessling and T. Lammers, *Adv. Drug Delivery Rev.*, 2019, **138**, 302–325.

7 S. Laurent, D. Forge, M. Port, A. Roch, C. Robic, L. Vander Elst and R. N. Muller, *Chem. Rev.*, 2008, **108**, 2064–2110.

8 M. Bilal, Y. Zhao, T. Rasheed and H. M. N. Iqbal, *Int. J. Biol. Macromol.*, 2018, **120**, 2530–2544.

9 M. H. Pablico-Lansigan, S. F. Situ and A. C. S. Samia, *Nanoscale*, 2013, **5**, 4040–4055.

10 Y. Li, N. Wang, X. Huang, F. Li, T. P. Davis, R. Qiao and D. Ling, *ACS Appl. Bio Mater.*, 2020, **3**, 121–142.

11 K. Wu, D. Su, J. Liu, R. Saha and J.-P. Wang, *Nanotechnology*, 2019, **30**, 502003.

12 R. C. Popescu, E. Andronescu and B. S. Vasile, *Nanomaterials*, 2019, **9**, 1791.

13 M. Basini, A. Guerrini, M. Cobianchi, F. Orsini, D. Bettega, M. Avolio, C. Innocenti, C. Sangregorio, A. Lascialfari and P. Arosio, *J. Alloys Compd.*, 2019, **770**, 58–66.

14 R. A. Bohara, N. D. Thorat and S. H. Pawar, *RSC Adv.*, 2016, **6**, 43989–44012.

15 S. Mornet, S. Vasseur, F. Grasset and E. Duguet, *J. Mater. Chem.*, 2004, **14**, 2161–2175.

16 V. L. Colvin, *Nat. Biotechnol.*, 2003, **21**, 1166–1170.

17 N. Lewinski, V. Colvin and R. Drezek, *Small*, 2008, **4**, 26–49.

18 B. Fadeel and A. E. Garcia-Bennett, *Adv. Drug Delivery Rev.*, 2010, **62**, 362–374.

19 C. Egbuna, V. K. Parmar, J. Jeevanandam, S. M. Ezzat, K. C. Patrick-Iwuanyanwu, C. O. Adetunji, J. Khan, E. N. Onyeike, C. Z. Uche, M. Akram, M. S. Ibrahim,

N. M. El Mahdy, C. G. Awuchi, K. Saravanan, H. Tijjani, U. E. Odoh, M. Messaoudi, J. C. Ifemeje, M. C. Olisah, N. J. Ezeofor, C. J. Chikwendu and C. G. Ibeabuchi, *J. Toxicol.*, 2021, **2021**, e9954443.

20 R. Abbasi, G. Shineh, M. Mobaraki, S. Doughty and L. Tayebi, *J. Nanopart. Res.*, 2023, **25**, 43.

21 M. Kaloyianni, A. Dimitriadis, M. Ovezik, D. Stamkopoulou, K. Feidantsis, G. Kastrinaki, G. Gallios, I. Tsiaoussis, G. Koumoundouros and D. Bobori, *J. Hazard. Mater.*, 2020, **383**, 121204.

22 K. Khanna, N. Sharma, P. Ohri and R. Bhardwaj, in *Plant and Nanoparticles*, Springer, Singapore, 2022, pp. 1–52.

23 A. Barhoum, M. L. García-Betancourt, J. Jeevanandam, E. A. Hussien, S. A. Mekkawy, M. Mostafa, M. M. Omran, M. S Abdalla and M. Bechelany, *Nanomaterials*, 2022, **12**, 177.

24 I. Castellanos-Rubio, O. Arriortua, L. Marcano, I. Rodrigo, D. Iglesias-Rojas, A. Barón, A. Olazagoitia-Garmendia, L. Olivi, F. Plazaola, M. L. Fdez-Gubieda, A. Castellanos-Rubio, J. S. Garitaonandia, I. Orue and M. Insausti, *Chem. Mater.*, 2021, **33**, 3139–3154.

25 X. Chu, J. Yu and Y.-L. Hou, *Chin. Phys. B*, 2015, **24**, 014704.

26 S. Venkateswarlu, B. Natesh Kumar, C. H. Prasad, P. Venkateswarlu and N. V. V. Jyothi, *Phys. B*, 2014, **449**, 67–71.

27 A. K. Das, A. Marwal and R. Verma, *Res. Rev.: J. Pharm. Nanotechnol.*, 2014, **2**, 21–24.

28 M. Shah, D. Fawcett, S. Sharma, S. Tripathy, G. Poinern, M. Shah, D. Fawcett, S. Sharma, S. K. Tripathy and G. E. J. Poinern, *Materials*, 2015, **8**, 7278–7308.

29 S. Kanagasubbulakshmi and K. Kadirvelu, *Def. Life Sci. J.*, 2017, **2**, 422.

30 N. Shreyash, S. Bajpai, M. A. Khan, Y. Vijay, S. K. Tiwary and M. Sonker, *ACS Appl. Nano Mater.*, 2021, **4**, 11428–11457.

31 M. Lazaratos, K. Karathanou, E. Mainas, A. Chatzigoulas, N. Pippa, C. Demetzos and Z. Cournia, *Biochim. Biophys. Acta, Gen. Subj.*, 2020, **1864**, 129671.

32 M. Yamazaki, in *Advances in Planar Lipid Bilayers and Liposomes*, Academic Press, 2008, vol. 7, pp. 121–142.

33 M. Z. Islam, J. M. Alam, Y. Tamba, M. A. S. Karal and M. Yamazaki, *Phys. Chem. Chem. Phys.*, 2014, **16**, 15752–15767.

34 R. Dimova and C. M. Marques, *The Giant Vesicle Book*, CRC Press, Taylor & Francis Group, 2019.

35 M. M. R. Moghal, F. Hossain and M. Yamazaki, *Biophys. Rev.*, 2020, **12**, 339–348.

36 M. Laurencin, T. Georgelin, B. Malezieux, J.-M. Siaugue and C. Ménager, *Langmuir*, 2010, **26**, 16025–16030.

37 S. Li and N. Malmstadt, *Soft Matter*, 2013, **9**, 4969–4976.

38 R. van der Meel, L. J. C. Vehmeijer, R. J. Kok, G. Storm and E. V. B. van Gaal, *Adv. Drug Delivery Rev.*, 2013, **65**, 1284–1298.

39 O. L. Gobbo, K. Sjaastad, M. W. Radomski, Y. Volkov and A. Prina-Mello, *Theranostics*, 2015, **5**, 1249–1263.

40 C. Alexiou, R. J. Schmid, R. Jurgons, M. Kremer, G. Wanner, C. Bergemann, E. Huenges, T. Nawroth, W. Arnold and F. G. Parak, *Eur. Biophys. J.*, 2006, **35**, 446–450.

41 L. Dykman and N. Khlebtsov, *Chem. Soc. Rev.*, 2012, **41**, 2256–2282.

42 A. K. Gupta and M. Gupta, *Biomaterials*, 2005, **26**, 3995–4021.

43 V. Pilati, G. Gomide, R. C. Gomes, G. F. Goya and J. Depeyrot, *Langmuir*, 2021, **37**, 1129–1140.

44 E. Piosik, A. Zaryczniak, K. Mylkie and M. Ziegler-Borowska, *Int. J. Mol. Sci.*, 2021, **22**, 5939.

45 E. Piosik, P. Klimczak, M. Ziegler-Borowska, D. Chełminiak-Dudkiewicz and T. Martyński, *Mater. Sci. Eng., C*, 2020, **109**, 110616.

46 R. Dimova, *Adv. Colloid Interface Sci.*, 2014, **208**, 225–234.

47 H. A. Faizi, S. L. Frey, J. Steinkühler, R. Dimova and P. M. Vlahovska, *Soft Matter*, 2019, **15**, 6006–6013.

48 R. Ashkar, M. Doktorova, F. A. Heberle, H. Scott, E. Kelley, M. Nagao, R. Usery, F. N. Barrera, G. W. Feigenson, J. Katsaras and G. Khelashvili, *Biophys. J.*, 2019, **116**, 328a.

49 M. A. S. Karal, M. M. Billah, M. Ahmed and M. K. Ahamed, *Soft Matter*, 2023, **19**, 8285–8304.

50 J. P. Reeves and R. M. Dowben, *J. Cell. Physiol.*, 1969, **73**, 49–60.

51 M. A. S. Karal, S. Ahammed, V. Levadny, M. Belaya, M. K. Ahamed, M. Ahmed, Z. B. Mahbub and A. K. M. A. Ullah, *Chem. Phys. Lipids*, 2020, **230**, 104916.

52 S. Hasan, M. A. S. Karal, S. Akter, M. Ahmed, M. K. Ahamed and S. Ahammed, *PLoS One*, 2022, **17**, e0275478.

53 M. A. S. Karal, S. Sultana, M. M. Billah, M. Moniruzzaman, M. A. Wadud and R. C. Gosh, *PLoS One*, 2023, **18**, e0289087.

54 M. Moniruzzaman, M. A. S. Karal, M. A. Wadud and M. M. O. Rashid, *Phys. Chem. Chem. Phys.*, 2023, **25**, 23111–23124.

55 Y. Tamba, H. Terashima and M. Yamazaki, *Chem. Phys. Lipids*, 2011, **164**, 351–358.

56 M. A. S. Karal, M. Rahman, M. K. Ahamed, S. U. A. Shibly, M. Ahmed and M. M. Shakil, *Eur. Biophys. J.*, 2019, **48**, 349–359.

57 A. Akbarzadeh, R. Rezaei-Sadabady, S. Davaran, S. W. Joo, N. Zarghami, Y. Hanifehpour, M. Samiei, M. Kouhi and K. Nejati-Koshki, *Nanoscale Res. Lett.*, 2013, **8**, 102.

58 M. M. Zaman, M. A. S. Karal, M. N. I. Khan, A. R. M. Tareq, S. Ahammed, M. Akter, A. Hossain and A. K. M. A. Ullah, *ChemistrySelect*, 2019, **4**, 7824–7831.

59 M. P. Calatayud, B. Sanz, V. Raffa, C. Riggio, M. R. Ibarra and G. F. Goya, *Biomaterials*, 2014, **35**, 6389–6399.

60 A. Fenster, *Ultrasound Med. Biol.*, 2001, **27**, 727.

61 J. C. W. Shepherd and G. Büldt, *Biochim. Biophys. Acta, Biomembr.*, 1978, **514**, 83–94.

62 M. Petrov, L. Cwiklik and P. Jungwirth, *Collect. Czech. Chem. Commun.*, 2011, **76**, 695–711.

63 A. Pabis, J. Szala-Bilnik and D. Swiatla-Wojcik, *Phys. Chem. Chem. Phys.*, 2011, **13**, 9458–9468.

64 M. A. S. Karal, M. Ahmed, V. Levadny, M. Belaya, M. K. Ahamed, M. Rahman and M. M. Shakil, *Phys. Rev. E*, 2020, **101**, 012404.

65 M. A. S. Karal, V. Levadnyy, T. Tsuboi, M. Belaya and M. Yamazaki, *Phys. Rev. E*, 2015, **92**, 012708.

66 M. A. S. Karal, U. S. Orchi, M. Towhiduzzaman, M. K. Ahamed, M. Ahmed, S. Ahammed, N. A. Mokta, S. Sharmin and M. K. Sarkar, *Chem. Phys. Lipids*, 2020, **231**, 104935.

67 J. N. Israelachvili, in *Intermolecular and Surface Forces*, Elsevier, 2011, pp. 291–340.

68 G. Cevc, *Phospholipid Bilayers: Physical Principles and Models*, Wiley, New York, 1987.

69 G. Cevc, *Biochim. Biophys. Acta, Rev. Biomembr.*, 1990, **1031**, 311–382.

70 M. Langner and K. Kubica, *Chem. Phys. Lipids*, 1999, **101**, 3–35.

71 R. Messina, *J. Phys.: Condens. Matter*, 2008, **21**, 199801.

72 H. J. Deuling and W. Helfrich, *J. Phys.*, 1976, **37**, 1335–1345.

73 O.-Y. Zhong-can and W. Helfrich, *Phys. Rev. Lett.*, 1987, **59**, 2486–2488.

74 H. J. Bohnert, D. E. Nelson and R. G. Jensen, *Plant Cell*, 1995, **7**, 1099–1111.

75 E. A. Bray, *Trends Plant Sci.*, 1997, **2**, 48–54.

76 P. H. Yancey, M. E. Clark, S. C. Hand, R. D. Bowlus and G. N. Somero, *Science*, 1982, **217**, 1214–1222.

77 L. M. Crowe, D. S. Reid and J. H. Crowe, *Biophys. J.*, 1996, **71**, 2087–2093.

78 M. d. C. Luzardo, F. Amalfa, A. M. Nuñez, S. Díaz, A. C. Biondi de Lopez and E. A. Disalvo, *Biophys. J.*, 2000, **78**, 2452–2458.

79 H.-G. Döbereiner, O. Selchow and R. Lipowsky, *Eur. Biophys. J.*, 1999, **28**, 174–178.

80 V. Vitkova, D. Mitkova, K. Antonova, G. Popkirov and R. Dimova, *Colloids Surf., A*, 2018, **557**, 51–57.

81 J. Genova, A. Zheliaskova and M. D. Mitov, *Colloids Surf., A*, 2006, **282–283**, 420–422.

82 J. F. Nagle, M. S. Jablin, S. Tristram-Nagle and K. Akabori, *Chem. Phys. Lipids*, 2015, **185**, 3–10.

83 V. Vitkova, J. Genova, M. D. Mitov and I. Bivas, *Mol. Cryst. Liq. Cryst.*, 2006, **449**, 95–106.

84 M. K. Sarkar, M. A. S. Karal, V. Levadny, M. Belaya, M. Ahmed, M. K. Ahamed and S. Ahammed, *Eur. Biophys. J.*, 2022, **51**, 401–412.

85 D. Venturoli and B. Rippe, *Am. J. Physiol.: Renal Physiol.*, 2005, **288**, F605–F613.

86 A. B. Goins, H. Sanabria and M. N. Waxham, *Biophys. J.*, 2008, **95**, 5362–5373.

87 Y. Tamba and M. Yamazaki, *J. Phys. Chem. B*, 2009, **113**, 4846–4852.

88 M. Hasan, M. A. S. Karal, V. Levadnyy and M. Yamazaki, *Langmuir*, 2018, **34**, 3349–3362.

89 M. K. Ahamed, M. A. S. Karal, M. Ahmed and S. Ahammed, *Eur. Biophys. J.*, 2020, **49**, 371–381.

90 I. J. Vereyken, V. Chupin, R. A. Demel, S. C. M. Smeekens and B. De Kruijff, *Biochim. Biophys. Acta, Biomembr.*, 2001, **1510**, 307–320.

91 R. A. Demel, E. Dorrepaal, M. J. M. Ebskamp, J. C. M. Smeekens and B. de Kruijff, *Biochim. Biophys. Acta, Biomembr.*, 1998, **1375**, 36–42.

92 A. Dhaliwal, A. Khondker, R. Alsop and M. C. Rheinstädter, *Membranes*, 2019, **9**, 15.

93 H. D. Andersen, C. Wang, L. Arleth, G. H. Peters and P. Westh, *Proc. Natl. Acad. Sci. U. S. A.*, 2011, **108**, 1874–1878.

94 J. W. DePierre and M. L. Karnovsky, *J. Cell Biol.*, 1973, **56**, 275–303.

95 S. Akter, M. A. S. Karal, S. Hasan, M. K. Ahamed, M. Ahmed and S. Ahammed, *RSC Adv.*, 2022, **12**, 28283–28294.

96 E. C. Giakoumatos, L. Gascoigne, B. Gumí-Audenis, Á. G. García, R. Tuinier and I. K. Voets, *Soft Matter*, 2022, **18**, 7569–7578.

97 A. Mahendra, H. P. James and S. Jadhav, *Chem. Phys. Lipids*, 2019, **218**, 47–56.

98 D. Marsh, R. Bartucci and L. Sportelli, *Biochim. Biophys. Acta, Biomembr.*, 2003, **1615**, 33–59.

99 L. Abdul Kadir, M. Stacey and R. Barrett-Jolley, *Front. physiol.*, 2018, **9**, 1661.

100 *Basic Neurochemistry: Principles of Molecular, Cellular, and Medical Neurobiology*, ed. S. T. Brady, G. J. Siegel, R. W. Albers and D. L. Price, Elsevier, Amsterdam, Paris, 8th edn, 2011.

101 J. P. Stratford, C. L. A. Edwards, M. J. Ghanshyam, D. Malyshev, M. A. Delise, Y. Hayashi and M. Asally, *Proc. Natl. Acad. Sci. U. S. A.*, 2019, **116**, 9552–9557.

102 A. Higuchi and T. Nakagawa, *J. Membr. Sci.*, 1987, **32**, 267–280.

103 M. M. R. Moghal, M. Z. Islam, F. Hossain, S. K. Saha and M. Yamazaki, *Biophys. J.*, 2020, **118**, 57–69.

104 F. Hossain, M. M. R. Moghal, M. Z. Islam, M. Moniruzzaman and M. Yamazaki, *J. Biol. Chem.*, 2019, **294**, 10449–10462.

105 F. Hossain, H. Dohra and M. Yamazaki, *J. Bacteriol.*, 2021, **203**, e00021.

106 T. Numata, T. Murakami, F. Kawashima, N. Morone, J. E. Heuser, Y. Takano, K. Ohkubo, S. Fukuzumi, Y. Mori and H. Imahori, *J. Am. Chem. Soc.*, 2012, **134**, 6092–6095.

107 A.-S. Feiner and A. J. McEvoy, *J. Chem. Educ.*, 1994, **71**, 493.

108 M. M. O. Rashid, M. M. R. Moghal, M. M. Billah, M. Hasan and M. Yamazaki, *Biochim. Biophys. Acta, Biomembr.*, 2020, **1862**, 183381.

109 E. Bamberg and P. Läuger, *J. Membr. Biol.*, 1973, **11**, 177–194.

110 A. Ring, *Biochim. Biophys. Acta, Biomembr.*, 1996, **1278**, 147–159.

111 J. A. Szule and R. P. Rand, *Biophys. J.*, 2003, **85**, 1702–1712.

112 S. Sundelacruz, M. Levin and D. L. Kaplan, *Stem Cell Rev. Rep.*, 2009, **5**, 231–246.

113 Y. Tamba, H. Ariyama, V. Levadny and M. Yamazaki, *J. Phys. Chem. B*, 2010, **114**, 12018–12026.

114 Y. Tamba and M. Yamazaki, *Biochemistry*, 2005, **44**, 15823–15833.

115 B. Wang, L. Zhang, S. C. Bae and S. Granick, *Proc. Natl. Acad. Sci. U. S. A.*, 2008, **105**, 18171–18175.

116 C. Contini, M. Schneemilch, S. Gaisford and N. Quirke, *J. Exp. Nanosci.*, 2018, **13**, 62–81.

117 F. Campelo and V. Malhotra, *Annu. Rev. Biochem.*, 2012, **81**, 407–427.

118 J. Käs and E. Sackmann, *Biophys. J.*, 1991, **60**, 825–844.

119 U. Seifert, K. Berndl and R. Lipowsky, *Phys. Rev. A*, 1991, **44**, 1182–1202.

120 V. Kralj-Iglič, V. Heinrich, S. Svetina and B. Žekš, *Eur. Phys. J. B*, 1999, **10**, 5–8.

121 S. J. Ludtke, K. He, W. T. Heller, T. A. Harroun, L. Yang and H. W. Huang, *Biochemistry*, 1996, **35**, 13723–13728.

122 F. Brochard-Wyart, P. G. de Gennes and O. Sandre, *Phys. A*, 2000, **278**, 32–51.

123 W. Rawicz, K. C. Olbrich, T. McIntosh, D. Needham and E. Evans, *Biophys. J.*, 2000, **79**, 328–339.

124 E. Evans, V. Heinrich, F. Ludwig and W. Rawicz, *Biophys. J.*, 2003, **85**, 2342–2350.

125 M. A. S. Karal, J. M. Alam, T. Takahashi, V. Levadny and M. Yamazaki, *Langmuir*, 2015, **31**, 3391–3401.

126 M. M. Billah, M. M. O. Rashid, M. Ahmed and M. Yamazaki, *Biochim. Biophys. Acta, Biomembr.*, 2023, **1865**, 184112.

127 N. Yoshida, M. Tamura and M. Kinjo, *Single Mol.*, 2000, **1**, 279–283.

128 E. Karatekin, O. Sandre, H. Guitouni, N. Borghi, P.-H. Puech and F. Brochard-Wyart, *Biophys. J.*, 2003, **84**, 1734–1749.

129 F. S. C. Leomil, M. Zoccoler, R. Dimova and K. A. Riske, *Bioinform. Adv.*, 2021, **1**, vbab037.

130 M. A. S. Karal, M. M. Billah and M. K. Ahamed, *Phys. Chem. Chem. Phys.*, 2024, **26**, 6107–6117.

131 J. D. Litster, *Phys. Lett. A*, 1975, **53**, 193–194.

132 V. Levadny, T. Tsuboi, M. Belaya and M. Yamazaki, *Langmuir*, 2013, **29**, 3848–3852.

133 S. A. Akimov, P. E. Volynsky, T. R. Galimzyanov, P. I. Kuzmin, K. V. Pavlov and O. V. Batishchev, *Sci. Rep.*, 2017, **7**, 12152.

134 S. A. Akimov, P. E. Volynsky, T. R. Galimzyanov, P. I. Kuzmin, K. V. Pavlov and O. V. Batishchev, *Sci. Rep.*, 2017, **7**, 12509.

135 D. Sengupta, H. Leontiadou, A. E. Mark and S.-J. Marrink, *Biochim. Biophys. Acta, Biomembr.*, 2008, **1778**, 2308–2317.

136 M.-T. Lee, T.-L. Sun, W.-C. Hung and H. W. Huang, *Proc. Natl. Acad. Sci. U. S. A.*, 2013, **110**, 14243–14248.

137 F. M. Kievit and M. Zhang, *Acc. Chem. Res.*, 2011, **44**, 853–862.

138 M. Mahmoudi, S. Laurent, M. A. Shokrgozar and M. Hosseinkhani, *ACS Nano*, 2011, **5**, 7263–7276.

139 O. C. Farokhzad and R. Langer, *ACS Nano*, 2009, **3**, 16–20.

140 J. Wolfram, M. Zhu, Y. Yang, J. Shen, E. Gentile, D. Paolino, M. Fresta, G. Nie, C. Chen, H. Shen, M. Ferrari and Y. Zhao, *Curr. Drug Targets*, 2015, **16**, 1671–1681.